Dynamical conductivity of a two-dimensional weakly doped Holstein system

Rukelj, Z.; Radić, D.; Krsnik, J.; Barišić, O. S.; Mishchenko, A. S.; Kupčić, I.

Dynamical conductivity of a two-dimensional weakly doped Holstein system

Z. Rukelj,[1,*] D. Radić,[1] J. Krsnik,[2,3] O. S. Barišić,[3] A. S. Mishchenko,[4] and I. Kupčić[1,†]

[1]*Department of Physics, Faculty of Science, University of Zagreb, Bijenička 32, 10000 Zagreb, Croatia*

[2]*Institute of Solid State Physics, TU Wien, 1040 Vienna, Austria*

[3]*Institute of Physics, Bijenička 46, 10000 Zagreb, Croatia*

[4]*RIKEN Center for Emergent Matter Science (CEMS), Wako, Saitama 351-0198, Japan*

(Received 27 July 2023; revised 19 September 2023; accepted 16 October 2023; published 30 October 2023)

The generalized Drude formula is used to study conductivity properties of the two-dimensional weakly doped Holstein model with a free-electron-like dispersion. The relaxation processes associated with the scattering of conduction electrons by optical phonons are described in terms of a frequency- and temperature-dependent memory function. The imaginary and real parts of the memory function are analyzed in detail in the regime when characteristic energy scales of the problem, i.e., electron Fermi energy and optical phonon energy, are comparable in size. Results obtained at zero temperature and at finite temperatures are used to determine temperature effects in the real part of the dynamical conductivity as well as the frequency dependence of the optical electron mass and the electron relaxation rate. Finally, the characteristic fingerprints of a Holstein system with multiple phonon branches are identified in the dynamical electron conductivity.

DOI: 10.1103/PhysRevB.108.155151

I. INTRODUCTION

In metallic systems in which conduction electrons are scattered by different types of dispersionless nonpolar boson modes, measured reflectivity spectra are usually analyzed in terms of a simple Drude-Lorentz formula. In this approach, there is one Drude term with frequency-independent relaxation rate [1] and several Lorentz contributions associated with different boson-assisted electron-hole excitations. The change in the doping level or in temperature usually leads to the redistribution of the conductivity spectral weight over a wide frequency range. This means that the electron-boson coupling plays an important role in an accurate description of both the electron relaxation rate(s) and the intensity of the Lorentz contribution(s).

The generalized Drude approach represents a model-independent method of analyzing the measured reflectivity spectra, which treats these two effects on an equal footing [2–4]. The frequency-dependent optical electron mass and the frequency-dependent relaxation rate extracted from the measured spectra are found to be related to the real and imaginary parts of the so-called memory function. The memory-function conductivity formula represents a theoretical model, derived from the quantum transport equations [5–7], which is a simple generalization of the generalized Drude formula to the case where the memory function depends on both frequency and wave vector. In this model, the memory function is nothing but the self-energy of an electron-hole pair created by an external long wavelength electromagnetic field of frequency ω. Also, the memory function approach can be extended to thermal transport as shown in [8].

It is well known that early treatments of the memory-function conductivity formula lead to the frequency-dependent memory function, which, in the static limit, gives the same expression for the relaxation rate as the common semiclassical approach [6,9]. A modern treatment of the memory-function conductivity formula based on the quantum transport equations gives a more accurate expression for the memory function even in the second-order perturbation theory [5,6]. Another advantage of the latter approach is that it makes possible calculations of higher-order contributions in perturbation theory by using the usual zero-temperature or finite-temperature diagrammatic rules. In a general case, the perturbation includes the scattering of conduction electrons by static disorder, [5,6,9–15] by other electrons, [6,9,16–18] or by different types of boson modes (acoustic and optical phonons, magnons, etc.) [9,19–21].

An important characteristic of the scattering by static disorder and by boson modes is that the second-order contribution to the memory function is comprised of four contributions. Two of them are the electron and hole self-energy contributions and two are related to the corresponding vertex corrections. When the later two contributions vanish for symmetry reasons, the second-order contribution to the memory function is simply the sum of the electron self-energy and the hole self-energy.

In this paper we study the basic conductivity properties of the two-dimensional (2D) weakly doped Holstein (wdH) model [22]. In this electron-phonon model, the coupling between conduction electrons and lattice vibrations does not depend on wave vectors. Moreover, in this doping range, the exact electron dispersion can be replaced by the parabolic (free-electron-like) dispersion. These simplifications lead to the second-order contribution to the memory function in which the vertex corrections vanish and the remaining two contributions can be evaluated analytically. This makes the

*zrukelj@phy.hr
†kupcic@phy.hr

comparison with other treatments of the Holstein problem much easier.

The Holstein model, with short-ranged electron-phonon interactions, has been a subject of intensive investigations for years. With corresponding modifications aimed to single out different aspects of real materials [23–25], this model permits a well-controlled analysis of the key behaviors governed by electron-phonon correlations. Indeed, in the most recent studies, new improvements in understanding electron and/or phonon spectral properties [26–28] have been reported. Similarly, using the Holstein model, thermalization, and transport properties [29–31] have been investigated recently as well.

Using the generalized intraband Drude conductivity formula, we look for the fingerprints of the wdH model in the dynamical conductivity as it evolves with doping and temperature. In the majority of conducting systems the Fermi energy is the dominant energy scale compared to the optical phonon energy $\hbar\omega_O$, incoming photon energy $\hbar\omega$, or temperature k_BT. This makes the evaluation of the memory function, which is the key ingredient of the dynamical conductivity, easier, yielding the simple analytical results [7,32]. However, in this paper we analyze the memory function properties when all four energy scales ε_F, $\hbar\omega_O$, $\hbar\omega$, and k_BT are comparable. In doing so, we use the well-known result for the electron-phonon memory function which was derived using the equation-of-motion technique for the electron-hole propagator [6,7]. We obtain a general expression for the memory function of 2D and three-dimensional (3D) wdH systems, evaluate it explicitly for a chosen 2D system, and finally provide the real part of the temperature- and frequency-dependent conductivity. The 2D wdH model will permit us to derive a few key results in a closed form. We also show that our approach may easily be used to numerically evaluate the conductivity for any electron dispersion.

In weakly doped electron-phonon coupled systems, the conductivity has been mostly analyzed in the context of the single-electron (polaron) problem. These results are obtained assuming that the system consists of a gas of fully independent (electrons) polarons [33,34], using the following technique: exact diagonalization techniques [27], diagrammatic expansion with neglected vertex corrections [35,36], density-matrix renormalization group methods [37,38], dynamical mean-field theory [39], kernel polynomial method [40], and momentum average approximation [31]. Based on recent experimental and theoretical insights [41–43], we adopt the electron-phonon weak-coupling picture in which we find that optical conductivity spectra exhibit sharp features from which the Fermi energy may be read directly.

Here, for the sake of presentation of a 2D system with presumably Holstein coupling, we take data for the MoS_2 monolayer, assuming just the order of magnitude of parameters without aiming to describe the features of that particular material. The conduction band of MoS_2, around its minimum located in the K point of the Brillouin zone, is well-approximated by a parabolic dispersion [44] and, in spite of the fact that additional complications arise due to the valley and spin degrees of freedom, this material has been a topic of multiple dynamical charge-transport studies [45–48].

The paper is structured as follows. In Sec. II we define the wdH Hamiltonian, the generalized Drude conductivity formula and the electron-phonon memory function. In Sec. III we give an operative expression for the imaginary part of the memory function for the 2D and 3D wdH systems. In Sec. IV we analyze the zero- and finite-temperature imaginary and real parts of the 2D wdH system memory function. The parameters used in evaluating the memory function are those corresponding to the 2D MoS_2 and the limits of the model applicability are defined. In Sec. V the real part of the generalized Drude conductivity is analyzed with the description of all relevant features in conductivity. A comparison with the extended Drude model is made and the intraband sum rule is defined. Finally, a case of a wdH system with multiple optical phonon branches is discussed.

II. WEAKLY DOPED HOLSTEIN MODEL AND GENERALIZED DRUDE FORMULA

Here we briefly describe the minimal Hamiltonian of the 2D and 3D wdH systems, as well as the main parts of the generalized Drude conductivity formula. The conducting electrons are described by a single-band spin-degenerate Hamiltonian

$$\hat{H}_{el} = \sum_{\mathbf{k}\sigma} \varepsilon_{\mathbf{k}} c^{\dagger}_{\mathbf{k}\sigma} c_{\mathbf{k}\sigma}, \tag{2.1}$$

with a parabolic-like dispersion $\varepsilon_{\mathbf{k}} = \hbar^2 k^2/2m^*$ where m^* is an effective mass. We assume only one longitudinal nonpolar optical phonon branch with the frequency ω_O, described by the Hamiltonian

$$\hat{H}_{ph} = \sum_{\mathbf{q}} \hbar\omega_O b^{\dagger}_{\mathbf{q}} b_{\mathbf{q}}, \tag{2.2}$$

coupled to electrons by the corresponding electron-phonon interaction

$$\hat{H}_{el-ph} = \frac{1}{\sqrt{N}} \sum_{\mathbf{k}\mathbf{k}'\sigma} G_{\mathbf{k}',\mathbf{k}} c^{\dagger}_{\mathbf{k}'\sigma} c_{\mathbf{k}\sigma} (b_{\mathbf{k}'-\mathbf{k}} + b^{\dagger}_{\mathbf{k}-\mathbf{k}'}). \tag{2.3}$$

In the above expression, N is the number of primitive cells and $G_{\mathbf{k}',\mathbf{k}}$ is electron-phonon coupling to the optical mode. The Holstein model approximates $G_{\mathbf{k}',\mathbf{k}} \approx G$. This choice of the optical phonon coupling parameter is backed by several *ab initio* studies of electron-phonon coupling in 2D [46,49] and 3D systems [50].

In general single-band metallic systems, the dynamical conductivity can be analyzed by using the generalized Drude conductivity formula [5–7]

$$\sigma_{\alpha\alpha}(\omega, T) = \frac{ie^2}{m_e} \frac{n_\alpha(T)}{\omega + M(\omega, T)}. \tag{2.4}$$

Here m_e is the bare electron mass, $M(\omega, T)$ is the memory function which includes all relevant electron scattering processes, and

$$n_\alpha(T) = \frac{2}{V} \sum_{\mathbf{k}} \left(-\frac{\partial \mathscr{F}_{\mathbf{k}}}{\partial \varepsilon_{\mathbf{k}}} \right) (m_e v^2_{\alpha\mathbf{k}}) \tag{2.5}$$

is the effective concentration of conduction electrons [1]. Index α determines the direction of the electric field and $v_{\alpha\mathbf{k}} = (1/\hbar)\partial\varepsilon_{\mathbf{k}}/\partial k_\alpha$ is the electron group velocity. For the zero-temperature ($T = 0$) case, the derivative of the Fermi-Dirac (FD) distribution $\mathscr{F}_{\mathbf{k}}$ in Eq. (2.5) is the Dirac δ-function,

i.e., $\partial \mathscr{F}_{\mathbf{k}}/\partial \varepsilon_{\mathbf{k}} = -\delta(\varepsilon_{\mathbf{k}} - \varepsilon_F)$. Also, for a parabolic band with effective mass m^*, there is a simple connection between the zero-temperature effective concentration $n_\alpha(0)$ and total concentration of electrons n: $n_\alpha(0)/m_e = n/m^*$. This property is exclusive for parabolic-like electron dispersion and does not hold in the general case [51,52].

When the conduction electrons are scattered only by one type of boson mode, the second-order perturbation theory gives the complex memory function which can be shown in the following compact form:

$$\begin{aligned} M(\omega, T) &\equiv \frac{1}{n_\alpha(T)}\frac{2}{V}\sum_{\mathbf{k}}\left(-\frac{\partial \mathscr{F}_{\mathbf{k}}}{\partial \varepsilon_{\mathbf{k}}}\right)\left(m_e v_{\alpha\mathbf{k}}^2\right) M(\mathbf{k}, \omega, T) \\ &= \frac{1}{n_\alpha(T)}\frac{2}{V}\sum_{\mathbf{k}}\left(-\frac{\partial \mathscr{F}_{\mathbf{k}}}{\partial \varepsilon_{\mathbf{k}}}\right)\left(m_e v_{\alpha\mathbf{k}}^2\right) \\ &\times \frac{(-1)}{N\hbar}\sum_{\mathbf{k}'}\sum_{s,s'=\pm 1}|G_{\mathbf{k}-\mathbf{k}'}|^2\left(1-\frac{v_{\alpha\mathbf{k}'}}{v_{\alpha\mathbf{k}}}\right) \\ &\times \frac{s\mathscr{N}(s\omega_{\mathbf{k}-\mathbf{k}'}) + s\mathscr{F}_{\mathbf{k}'}}{\hbar\omega + s'(\varepsilon_{\mathbf{k}} - \varepsilon_{\mathbf{k}'}) + ss'\hbar\omega_{\mathbf{k}-\mathbf{k}'} + i\epsilon}. \end{aligned} \tag{2.6}$$

In the above definition the indices $s, s' = \pm 1$ and the property of the Bose-Einstein (BE) distribution $-\mathscr{N}(-\omega_{\mathbf{k}-\mathbf{k}'}) = 1 + \mathscr{N}(\omega_{\mathbf{k}-\mathbf{k}'})$ are used to put the expression in a compact form. Also, ϵ is an infinitesimal constant. Causality requirements on the conductivity (2.4) impose constraints on the imaginary $M_2(\omega, T) = M_2(-\omega, T)$ and real $M_1(\omega, T) = -M_1(-\omega, T)$ parts of the memory function (2.6). This further implies that the two parts are connected by the Kramers-Kronig relations (KKR). At this point caution is in order regarding the second-order perturbation theory for $M(\omega, T)$. This approximation is usually believed to be a good approximation in heavily doped 2D and 3D systems. However, in the wdH model (in weakly doped 2D MoS_2 as well [53]) it may be better to replace $M(\mathbf{k}, \omega, T)$ in Eq. (2.6) by its Hartree-Fock form [6] in which higher-order self-energy contributions are taken into account through the electron and phonon spectral functions. This leads to the renormalization of FD and BE distributions [54].

III. MEMORY FUNCTION OF THE WDH MODEL

In this section, the imaginary part of the memory function (2.6) is evaluated for both the 2D and 3D cases as a function of an incoming photon energy which we designate by $\Omega = \hbar\omega$. The three variables, the incoming photon energy Ω, the Fermi energy ε_F, and the optical phonon energy $\Omega_O = \hbar\omega_O$, are all comparable in magnitude to each other. Implementing the new variables Ω and Ω_O into the imaginary part of Eq. (2.6) gives

$$\begin{aligned} M_2(\Omega, T) &= \frac{2\pi m_e}{\hbar n_\alpha(T) V N}|G|^2\sum_{\mathbf{k}}\left(-\frac{\partial \mathscr{F}_{\mathbf{k}}}{\partial \varepsilon_{\mathbf{k}}}\right) \\ &\times \sum_{\mathbf{k}'}\left(v_{\alpha\mathbf{k}}^2 - v_{\alpha\mathbf{k}}v_{\alpha\mathbf{k}'}\right) \\ &\times \sum_{s,s'=\pm 1} s[\mathscr{N}(s\Omega_O) + \mathscr{F}(\varepsilon_{\mathbf{k}'})] \\ &\times \delta(\Omega + s'(\varepsilon_{\mathbf{k}} - \varepsilon_{\mathbf{k}'}) + ss'\Omega_O). \end{aligned} \tag{3.1}$$

The δ-function in Eq. (3.1) is a consequence of energy conservation. The contributions related with the first and the second terms in $(v_{\alpha\mathbf{k}}^2 - v_{\alpha\mathbf{k}}v_{\alpha\mathbf{k}'})$ are usually called the single-electron self-energy contribution and the related vertex corrections. Since the electron dispersion (2.1) is isotropic, all components $\alpha \in (x, y)$ are equivalent, hence $v_{\alpha\mathbf{k}}v_{\alpha\mathbf{k}'} \propto \mathbf{k}\cdot\mathbf{k}'$. However, within the δ-function in Eq. (3.1), there is no dependence on the angle between vectors $\mathbf{k}$ and $\mathbf{k}'$, only on their magnitudes which are contained within electron energies $\varepsilon_{\mathbf{k}}$ and $\varepsilon_{\mathbf{k}'}$. Since the FD distribution derivative is also isotropic, the angular integration of $\mathbf{k}\cdot\mathbf{k}'$ within $\sum_{\mathbf{k},\mathbf{k}'}$ will vanish. Therefore, in the present wdH model the vertex corrections in $M_2(\Omega, T)$ vanish. This would not have been the case if we where calculating the imaginary part of the memory function for acoustic phonon [7]. For acoustic case $\Omega_{\mathbf{k}-\mathbf{k}'} \propto |\mathbf{k} - \mathbf{k}'|$, the angular integration is restricted by the δ-function, or the energy conservation requirement, and the $\mathbf{k}\cdot\mathbf{k}'$ term does not vanish but gives the $\cos\angle(\mathbf{k}, \mathbf{k}')$ contribution to the resistivity instead [55]. Similarly, the term $v_{\alpha\mathbf{k}}^2 \sim k_\alpha^2$, after the angular integration is performed, is found to be connected with the D-dimensional electron dispersion as $v_{\alpha\mathbf{k}}^2 \to v_{\mathbf{k}}^2/D = 2\varepsilon_{\mathbf{k}}/(Dm^*)$.

The final shape of the Eq. (3.1) will be given in the energy representation. For this purpose, we introduce the density of states (DOS) per unit volume for a $D \in (2, 3)$-dimensional free-electron-like system

$$\nu(\varepsilon) = \frac{m^*}{\pi^{D-1}\hbar^D}(2m^*\varepsilon)^{(D-2)/2}\,\Theta(\varepsilon), \tag{3.2}$$

where $\Theta(\varepsilon)$ is the Heaviside unit step function and ε is energy. Using the identities like $\delta(s\varepsilon_{\mathbf{k}}) = \delta(\varepsilon_{\mathbf{k}})/|s|$ and $s^2 = s'^2 = 1$, we can rewrite the δ-function in Eq. (3.1) in the form

$$\delta(\varepsilon_{\mathbf{k}} + s'\Omega + s\Omega_O - \varepsilon_{\mathbf{k}'}). \tag{3.3}$$

Thus, Eq. (3.1) becomes

$$\begin{aligned} M_2(\Omega, T) &= \frac{\pi m_e}{Dm^*}\frac{v_{pc}|G|^2}{\hbar n_\alpha(T)}\int_0^\infty d\varepsilon\,\varepsilon\,\nu(\varepsilon)\left(-\frac{\partial \mathscr{F}(\varepsilon)}{\partial \varepsilon}\right) \\ &\times \sum_{s,s'=\pm 1} s\,\nu(\varepsilon + s'\Omega + s\Omega_O) \\ &\times [\mathscr{N}(s\Omega_O) + \mathscr{F}(\varepsilon + s'\Omega + s\Omega_O)]. \end{aligned} \tag{3.4}$$

In the above expression a primitive cell volume (area) $v_{pc} = V/N$ is introduced. What would have been the second integral over ε' in Eq. (3.4) was canceled by the δ-function (3.3) with the allowed ε' values transferred to the DOS and the FD distribution. Also, due to the Θ-function in the density of states (3.2), an additional constraint appears

$$\varepsilon' = \varepsilon + s'\Omega + s\Omega_O \geqslant 0. \tag{3.5}$$

The approach outlined in deriving (3.4) is easily generalized to other Holstein-like systems with isotropic electron dispersion. One has to find the DOS of a system, the effective concentration, as well as the square of velocity as a function of electron dispersion, i.e., $v_{\mathbf{k}}^2 = f(\varepsilon_{\mathbf{k}})$ and plug them into Eq. (3.4).

As noted in Sec. II, the real and imaginary parts of the memory function are connected via KKR. Hence, we get the

real part by evaluating the integral

$$M_1(\Omega, T) = \frac{1}{\pi}\int_{-\infty}^{\infty} \frac{M_2(\Omega', T)}{\Omega' - \Omega} d\Omega'. \tag{3.6}$$

As will be shown, only in the 2D zero-temperature case can we obtain a closed analytical expression for $M_1(\Omega, 0)$ and $M_2(\Omega, 0)$. On the other hand, for finite temperatures, a numerical evaluation is necessary.

We now proceed to evaluate the zero- and finite-temperature memory functions for a 2D test system.

IV. 2D WDH MEMORY FUNCTION

The test system for the wdH memory function evaluation comprises parameters from electron-doped MoS_2 monolayer with the primitive cell area $v_{pc} = a^2\sqrt{3}/2$, where $a = 3.14$ Å is the lattice constant. The bottom of the conduction band is located in the K point of the Brillouin zone around which the electron dispersion can be approximated by a parabola with an effective mass $m^* = 0.5\, m_e$ [44]. It is assumed that the Fermi energy ε_F can be changed by doping and is measured from the bottom of the conduction band. In Eq. (3.4) we insert the corresponding 2D DOS (3.2) and the effective concentration (2.5) which for the 2D electrons with dispersion (2.1) does not depend on temperature and is equal to

$$n_\alpha = \frac{m_e \varepsilon_F}{\pi \hbar^2}. \tag{4.1}$$

Finally, a version of Eq. (3.4) for the 2D wdH system becomes

$$\begin{aligned} M_2(\Omega, T) = \lambda \sum_{s,s'=\pm 1} \int_0^\infty d\varepsilon \, \frac{\varepsilon}{\varepsilon_F} \left(-\frac{\partial \mathscr{F}(\varepsilon)}{\partial \varepsilon} \right) \\ \times \Theta(\varepsilon + s'\Omega + s\Omega_O) \\ \times s[\mathscr{N}(s\Omega_O) + \mathscr{F}(\varepsilon + s'\Omega + s\Omega_O)]. \end{aligned} \tag{4.2}$$

The constant λ has the units of s^{-1} and is equal to

$$\lambda = \frac{v_{pc} m^*}{2\hbar^3} |G|^2 = \frac{1}{\varepsilon_T} \frac{|G|^2}{\hbar \omega_O} \omega_O = \lambda_0 \omega_O. \tag{4.3}$$

In Eq. (4.3) we expressed λ through a dimensionless coupling constant λ_0, usually found in the polaron analysis [56], and the phonon frequency ω_O. The denominator in the second term in Eq. (4.3) is the electron energy scale $\varepsilon_T = 2\hbar^2/(m^* v_{pc})$, which for the MoS_2 monolayer is around $\varepsilon_T \approx 3.55$ eV. Combined with the optical phonon energy $\Omega_O \approx 50$ meV [57] we get the following constraint: to make $\lambda_0 < 1$, which defines the weak coupling regime where Eq. (2.4) is applicable, G has to be $G < 0.4$ eV.

In the expression (4.2) which is to be evaluated for temperatures comparable to ε_F, it is necessary to include the temperature dependence of the electron chemical potential within the FD distributions. For the 2D electrons described by a single parabolic band, we use the well-known expression

$$\mu(T) = k_B T \ln\left[\exp(\varepsilon_F / k_B T) - 1\right]. \tag{4.4}$$

Now we consider the $T = 0$ limit of expression (4.2) providing a simple analytical solution that follows.

A. Zero-temperature 2D wdH memory function

Setting $T = 0$ in Eq. (4.2) the integral reduces to the $\varepsilon = \varepsilon_F$ value of its subintegral function, which, combined with the $T = 0$ value of the BE and FD distributions (in the form of the Θ-function and Kronecker δ-symbol), gives

$$\begin{aligned} M_2(\Omega, 0) = \lambda \sum_{s,s'=\pm 1} s[\delta_{s,+} - \Theta(s'\Omega + s\Omega_O)] \\ \times \Theta(\varepsilon_F + s'\Omega + s\Omega_O). \end{aligned} \tag{4.5}$$

The above expression is valid under the constraint (3.5) which now becomes

$$\varepsilon_F + s'\Omega + s\Omega_O > 0. \tag{4.6}$$

Assuming that initially $\varepsilon_F > \Omega_O$, it is easy to check the allowed positive Ω-values from Eq. (4.6) for every (s, s') pair. The $(+,+)$ case is valid $\forall\Omega$, case $(+,-)$ is valid if $\Omega < \varepsilon_F + \Omega_O$, case $(-,+)$ is valid $\forall\Omega$, and finally case $(-,-)$ is valid if $\Omega < \varepsilon_F - \Omega_O$. These restrictions on Ω make Eq. (4.5) a piecewise function

$$M_2(\Omega, 0) = \lambda \times \begin{cases} 0, & \Omega < \Omega_O, \\ 2, & \Omega_O < \Omega < \Omega_R, \\ 1, & \Omega_R < \Omega, \end{cases} \tag{4.7}$$

where we introduce $\Omega_R = \Omega_O + \varepsilon_F$. Furthermore, an additional dimensionless parameter $\eta = \varepsilon_F/\Omega_O$ is introduced for making the future analysis independent of the specific values of Ω_O and ε_F. $M_2(\Omega, 0)$, Eq. (4.7), is shown in Fig. 1 in red, as a function of Ω, for cases $\eta = 2$ and $\eta = 0.2$ in units of λ. The main feature is the absence of scattering for $\Omega < \Omega_O$, followed by the maximal and a constant value for $\Omega < \Omega_R$, and half that much for $\Omega > \Omega_R$.

As noted in Sec. II, the real and imaginary parts of the memory function are connected via KKR. Since $M_2(\Omega, 0)$ is an even function we can easily include the negative values of Ω in the expression (4.7) and, after inserting it into Eq. (3.6), we obtain

$$M_1(\Omega, 0) = \frac{\lambda}{\pi} \ln\left| \left(\frac{\Omega_R - \Omega}{\Omega_R + \Omega}\right) \left(\frac{\Omega_O + \Omega}{\Omega_O - \Omega}\right)^2 \right|. \tag{4.8}$$

The real part of the memory function is shown in the Fig. 1 in blue, as a function of Ω, in units of λ. There are several notable features of $M_1(\Omega)$, some of which depend on whether or not $\eta > 1$. The two logarithmic singularities of opposite signs are located at the discontinuity of $M_2(\Omega, 0)$. In the $\Omega \ll \Omega_O$ limit, Eq. (4.8) can be expanded to give an approximate expression

$$M_1(\Omega \ll \Omega_O, 0) \approx \frac{2\lambda}{\pi} \frac{1 + 2\eta}{1 + \eta} \frac{\Omega}{\Omega_O}. \tag{4.9}$$

Expression (4.9) will give a renormalized value of the dynamical effective mass in the far infrared frequency range. Also, in the large $\Omega \gg \Omega_R$ limit, Eq. (4.8) reduces to

$$M_1(\Omega \gg \Omega_R, 0) \approx \frac{2\lambda}{\pi}(1 - \eta)\frac{\Omega_O}{\Omega}. \tag{4.10}$$

From Eq. (4.10) we see that if $\eta > 1$, then $M_1(\Omega \gg \Omega_R, 0)$ approaches zero from below Fig. 1(a). This large Ω behavior is closely connected with the zero points Ω_z where the real part of the memory function vanishes, i.e., $M_1(\Omega_z, 0) = 0$. If $\eta > 1$, then $M_1(\Omega, 0)$ has a single zero-point

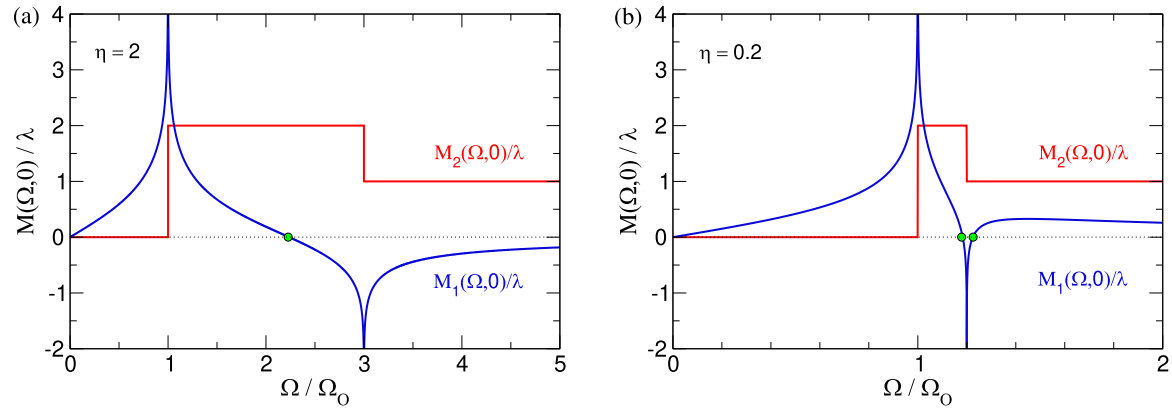

FIG. 1. (a) The real M_1 (4.8) (blue) and the imaginary part M_2 (4.7) (red) of the memory function in units of λ (4.3) as a function of scaled photon energy in units of Ω_O at zero temperature. In these scaled units, the position of Ω_R is located at $\Omega_R/\Omega_O = 1+\eta$. The Fermi energy is $\varepsilon_F = 2\Omega_O$, making $\eta = 2$. (b) Identical labeling of the memory function parts like in the (a) case plotted for $\varepsilon_F = 0.2\Omega_O$ which gives $\eta = 0.2$. In both figures the zero points of the real part of the memory function are indicated by the green dots.

$\Omega_z = \Omega_O\sqrt{1+2\eta}$, Fig. 1(a). If $\eta < 1$, an additional zero-point appears at $\Omega_z = \Omega_O\sqrt{(1+\eta)/(1-\eta)}$, as shown in Fig. 1(b).

Here is a good place to mention the constraints under which the presented model of the memory function applies. In the $T \approx 0$ case, the derivative of the FD distribution in Eq. (3.4) localizes the initial electron momentum $k \sim \sqrt{\varepsilon}$ on the Fermi surface $k \approx k_F$, while the scattered electron momentum $k' \sim \sqrt{\varepsilon'}$ (3.5) is evidently unbound in magnitude. This is seen on the $(s, s') = (+,+)$ example of Eq. (3.5) where, if Ω is arbitrarily large, so is ε'. This is so because there is no constraint on the angular dependence between vectors $(\mathbf{k}, \mathbf{k}')$, which enables us to derive Eq. (3.4). However, the difference between the incoming and scattered electron momenta should be less than the "Debye wave number" q_D, a radius of a circle with an area equal to the Brillouin zone. For the 2D MoS_2, $q_D = \sqrt{4\pi/v_{pc}}$ [7] so the restriction is simply $|\mathbf{k}_F - \mathbf{k}'| < q_D$. Taking a square and multiplying this inequality by $\hbar^2/2m^*$ we get

$$\varepsilon_F - 2\sqrt{\varepsilon_F\varepsilon'}\cos\varphi + \varepsilon' < \varepsilon_D, \tag{4.11}$$

where φ is an angle between vectors $(\mathbf{k}_F, \mathbf{k}')$, ε' is given by Eq. (3.5), and ε_D is the electron energy scale associated with the "Debye wave number." It is easy to check that ε_D is of the same order of magnitude as the electron energy scale ε_T. If the energies ε_F and ε_D are comparable, then a restriction on the allowed values of the angle φ from Eq. (4.11) would have to be imposed on Eq. (3.4) for every (s, s') pair, which would make the present analysis much more complicated. However, if $\Omega \approx \Omega_O \approx \varepsilon_F \ll \varepsilon_D$, then inequality (4.11) is obeyed for all φ and the evaluation of Eq. (4.5) as it is performed is exact. The same argument applies if the electron-phonon coupling in Eq. (2.3) is $G_{\mathbf{k}',\mathbf{k}} = G\,\Theta(q_D - |\mathbf{k}' - \mathbf{k}|)$, with q_D now an arbitrary constant whose associated energy ε_D obeys Eq. (4.11).

B. Finite-temperature 2D wdH memory function

Due to the complexity of Eq. (4.2) the properties of the finite-temperature memory function are calculated numerically. We investigate how the memory function depends on the scaled photon energy Ω and whether or not ε_F is bigger or smaller than Ω_O ($\eta > 1$ and $\eta < 1$). To this goal we introduce $\theta \equiv k_BT/\Omega_O$ as the dimensionless thermal energy scale. Taking the KKR (3.6) of Eq. (3.4), $M_1(\Omega,\theta)$ is obtained. For $\theta \ll 1$ at photon energies $\Omega = \Omega_O$ and $\Omega = \Omega_R$, the step feature in $M_2(\Omega,\theta)$ smears, producing a finite slope of width $\sim 1/\theta$, Figs. 2(a) and 2(c). The appearance of a finite slope in M_2 removes the zero-temperature logarithmic singularity in M_1 at points Ω_O and Ω_R in favor of the $M_1 \sim \lambda\ln\theta$ type of behavior, Figs. 2(b) and 2(c). The approximate model of a $\theta \ll 1$ memory function is given in the Appendix.

As θ increases, so does the amplitude of a static $M_2(0,\theta)$ part and eventually the step-like feature between the points Ω_O and Ω_R smooths out. The temperature dependence of $M_2(0,\theta)$ is shown in several approximations in Fig. 2(d). If the derivative of the FD distribution in Eq. (4.2) is approximated by a δ-function with $\mu(T) = \varepsilon_F$, the static part is equal to

$$M_2(0,\theta) = \frac{4\lambda}{\sinh(1/\theta)}, \tag{4.12}$$

which is shown in Fig. 2(d) as a black line and is clearly independent of ε_F. Equation (4.12) is to be compared with the exact result (4.2) with $\mu(T)$ for $\eta = 2$ (blue full line) and $\eta = 0.2$ (red full line). Also, the approximate result with $\mu(T) = \varepsilon_F$ is shown as the dashed blue and red lines on the same figure for corresponding values of η. The discrepancy in $M_2(0,\theta)$, whether it has been calculated with exact $\mu(T)$ or constant ε_F, becomes bigger the smaller ε_F is, as seen in Fig. 2(d) where the deviation between the full and dashed lines begins on lower values of θ for lower ε_F. Also, the presence of the temperature-shifting chemical potential, as well as the temperature broadening of the FD distribution derivative, do not alter the classical $M_2(0,\theta) \sim \theta$ result for large-θ values [58]. Next we regard the finite θ and the large Ω limit of $M_2(\Omega,\theta)$. By large Ω limit we mean $\Omega \gg \Omega_R$ under the constraint of the applicability of the model as explained in Sec. IV A. Then, Eq. (4.2) reduces to

$$M_2(\Omega \gg \Omega_R, \theta) \approx 2\lambda[\mathcal{N}(1/\theta) + 1/2], \tag{4.13}$$

which is proportional to an occupancy of the harmonic oscillator in the heat bath as shown in Fig. 2(d). Setting $\theta = 0$ in Eq. (4.13) we recover Eq. (4.7) while for large-enough θ

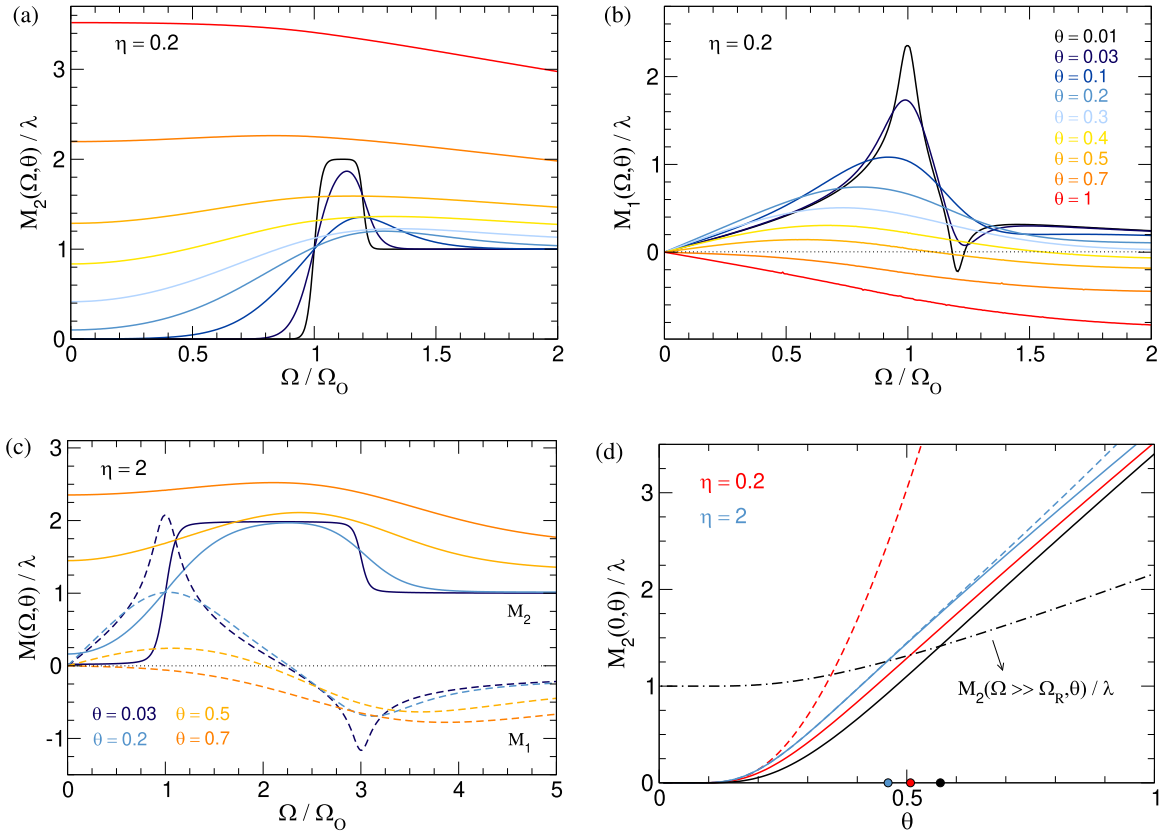

FIG. 2. (a,b) The imaginary M_2 and real M_1 parts of the memory function for $\eta = 0.2$ as functions of photon energy Ω in units of λ plotted for the same values of θ defined in (b). (c) The imaginary (full lines) and real (dashed lines) part of the memory function as a function of photon energy Ω in units of λ, plotted for several values of θ, for the case $\eta = 2$. (d) The temperature dependence of the static part of the memory function, for the two cases of η, in units of λ. Solid red and blue lines represent the case when the exact electron chemical potential $\mu(T)$ in Eq. (4.2) is used, while the dashed lines present the approximate result for $\mu(T) = \varepsilon_F$. The solid black line is Eq. (4.12) and the dot-dashed line is Eq. (4.13). The blue and a red dots show $\theta_s(2)$ and $\theta_s(0.2)$ while the black dot gives θ_s.

it gives $M_2(\Omega \gg \Omega_R, \theta) \sim \theta$ as does its static analog (4.12). There is a specific η-dependent temperature $\theta_s(\eta)$ at which $M_2[0, \theta_s(\eta)] = M_2[\Omega \gg \Omega_R, \theta_s(\eta)]$ as shown in Fig. 2(d), which is located bellow $\theta_s = 0.567$ obtained from the approximate expressions (4.12) and (4.13).

$M_1(\Omega, \theta)$ is shown in Figs. 2(b) and 2(c). Regardless of parameter η, two features of $M_1(\Omega, \theta)$ stand out. The first one is a monotonically decreasing high-energy value of $M_1(\Omega > \Omega_R, \theta)$ as θ increases. The second one is the non-monotonic θ-dependence of the low-energy slope of $M_1(\Omega < \Omega_O, \theta)$. Besides being the real part of the electron-hole pair self-energy, in Sec. V A another meaning to $M_1(\Omega, \theta)$ will be assigned. There it will define the dynamical effective mass of the electron participating in the charge transport and show how the thermal bath of optical Holstein phonons influences the mass of the conducting electrons, making it lighter or heavier depending on the driving frequency of the external electromagnetic field.

V. DYNAMICAL CONDUCTIVITY OF 2D WDH SYSTEM

The dynamical conductivity, as given by the generalized Drude formula (2.4), is evaluated as a function of photon energy Ω and temperature θ. After the effective concentration n_α, Eq. (4.1), is inserted in Eq. (2.4), the generalized Drude formula becomes

$$\sigma(\Omega, \theta) = \sigma_0 \frac{i\varepsilon_F}{\Omega + \hbar M_1(\Omega, \theta) + i\hbar M_2(\Omega, \theta) + i\gamma}, \quad (5.1)$$

where $\sigma_0 = e^2/(\pi\hbar)$ is the conductivity constant and $M_{1,2}(\Omega, \theta)$ are the real and imaginary parts of the memory function (3.6) and (4.2). To ensure a finite height of the zero-frequency Drude peak for $\Omega < \Omega_O$ and $\theta = 0$, a constant residual scattering $\gamma = 0.01\Omega_O$ has been introduced. Such residual scattering can be justified by the everlasting presence of a static disorder in the system.

First, we inspect the real part of conductivity (5.1)

$$\sigma_1(\Omega, \theta) = \sigma_0 \frac{\varepsilon_F[\hbar M_2(\Omega, \theta) + \gamma]}{[\Omega + \hbar M_1(\Omega, \theta)]^2 + [\hbar M_2(\Omega, \theta) + \gamma]^2}, \quad (5.2)$$

in the $\theta = 0$ case. $\sigma_1(\Omega, 0)$ is shown in Fig. 3(a) as function of Ω for $\varepsilon_F = \Omega_O$ (or $\eta = 1$) and for several values of a coupling parameter λ_0. $\sigma_1(\Omega, 0)$ has a hump-like onset at a photon energy equal to Ω_O. When $\Omega < \Omega_O$, there is no relaxation, apart from the arbitrarily small constant γ, thus $\sigma_1(\Omega, 0) \propto \gamma/(\Omega^2 + \gamma^2)$ in this frequency interval and vanishes if $\gamma = 0$. As $\Omega = \Omega_O$ is reached, a finite value of $M_2(\Omega_O, 0)$ makes $\sigma_1(\Omega_O, 0)$ finite. The spike in $\sigma_1(\Omega, 0)$ located near Ω_R has an intricate structure. If we zoom-in the scale, as shown in

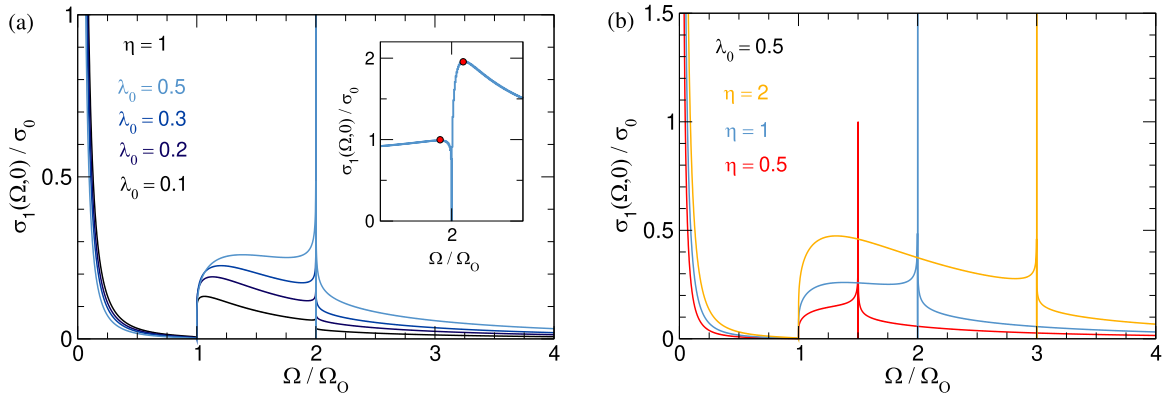

FIG. 3. (a) The real part of the zero-temperature dynamical conductivity, Eq. (5.2), in units of $\sigma_0 = e^2/(\pi\hbar)$, calculated for $\varepsilon_F = \Omega_O$, and for several values of coupling λ_0 (4.3), as a function of photon energy Ω. The inset shows a zoomed-in section of the $\sigma_1(\Omega, 0)$, calculated with $\lambda_0 = 0.5$ in the proximity of Ω_R, with the conductivity at two points $\Omega^*_{1,2}$ denoted by red circles. (b) The real part of the zero-temperature dynamical conductivity, Eq. (5.2), in units of σ_0, calculated for $\lambda_0 = 0.5$, and for several values of parameter η as a function of photon energy Ω. In both figures the residual scattering relaxation constant is $\gamma = 0.01\Omega_O$.

the inset in Fig. 3(a), we see that the spike is, in fact, comprised of three very close points. In the center there is the point Ω_R, at this particular point $M_1(\Omega_R, 0)$ diverges, and so the conductivity vanishes $\sigma_1(\Omega_R, 0) = 0$. This, however, is difficult to observe since $\sigma_1(\Omega, 0)$ goes to zero near Ω_R as a reciprocal square of the logarithm. Around photon energy equal to Ω_R, the two points $\Omega^*_{1,2}$ are positioned, which obey $\Omega^* + \hbar M_1(\Omega^*, 0) = 0$. At these points, as can be seen from the inset Fig. 3(a), σ_1 is finite and equal to $\sigma_1(\Omega^*_{1,2}, 0) = \sigma_0\varepsilon_F/\hbar M_2(\Omega^*_{1,2}, 0)$. Since $\Omega^*_1 < \Omega_R$ and $\hbar M_2(\Omega^*_1, 0) = 2\lambda_0\Omega_O$ and correspondingly $\Omega^*_2 > \Omega_R$ and $\hbar M_2(\Omega^*_2, 0) = \lambda_0\Omega_O$ as given by Eq. (4.7), the spike height around Ω_R is

$$\sigma_1(\Omega^*_2, 0) = \sigma_0 \frac{\eta}{\lambda_0}. \tag{5.3}$$

Although the spike height is larger for the low λ_0 values, implying it should be a dominate feature of the zero-temperature optical response of the wdH system, the width of the spike exponentially decreases. After some trivial algebra, it is easy to show that $|\Omega^*_2 - \Omega^*_1| \propto \Omega_R e^{-\pi/\lambda_0}$, making it unobservable even at zero temperatures, or even for a relatively large $\lambda_0 = 0.5$, since $|\Omega^*_2 - \Omega^*_1|/\Omega_R \sim 10^{-4}$. These peculiar zero-temperature features around Ω_R of any response function assembled from $M_{1,2}(\Omega, 0)$ shall be encountered further in the paper.

As λ_0 increases, the spectral weight of the intraband charge carriers is being transferred from the Lorentzian-like part located below $\Omega < \Omega_O$, to the parts above $\Omega > \Omega_O$ as seen from Fig. 3(a). This is due to the intraband spectral weight conservation, which, for the particular case of conductivity Eq. (5.1), gives

$$\int_0^\infty \sigma_1(\Omega, \theta)\, d\Omega = \frac{\pi}{2}\sigma_0\varepsilon_F, \tag{5.4}$$

regardless of the value of λ_0 (4.3) or the temperature θ. This is a natural consequence of the shape of the conductivity Eq. (5.1) featuring the memory function and the KKR connecting its real and imaginary parts. To see that the sum rule Eq. (5.4) holds, in Fig. 3(b) the real part of the conductivity is plotted for three values of the Fermi energy (parameter η) and the same coupling λ_0. The hump in the conductivity not only increases its amplitude with increasing η, but also expands to the right since the spike position is near Ω_R. Again, the area under the curves in Fig. 3(b) obeys the sum rule Eq. (5.4).

The two visible effects of increasing temperature in $\sigma_1(\Omega, \theta)$ are the removal of the spike at Ω_R and shifting of spectral weight to lower frequencies thus "filling the void" below Ω_O as shown in Fig. 4. Increasing the temperature above $\theta_s(\eta)$ defined in Sec. IV B gives $\sigma_1(\Omega, \theta)$ a wide Lorentzian-like shape from which the memory function features are not visible anymore. Another feature is the temperature-dependent static conductivity, or its inverse, the DC resistivity. Setting $\gamma = 0$ from Eq. (5.2) we get

$$\rho(\theta) = \frac{\hbar M_2(0, \theta)}{\sigma_0\varepsilon_F}, \tag{5.5}$$

which is shown in Fig. 2(d) since $\rho(\theta)$ is proportional to the static θ-dependent memory function.

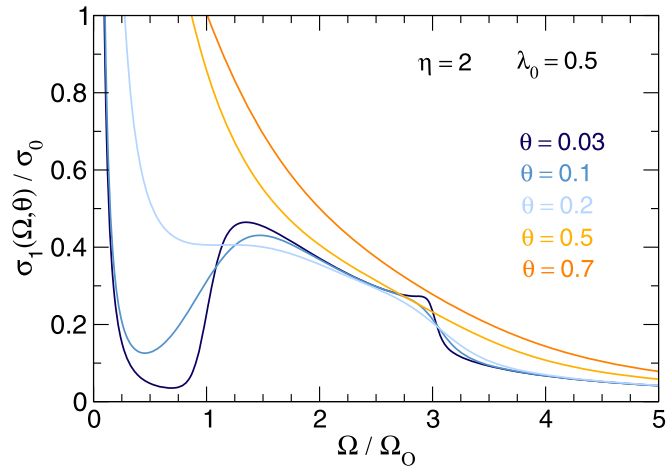

FIG. 4. The real part of the dynamical conductivity, Eq. (5.2), as a function of photon energy Ω, in units of $\sigma_0 = e^2/(\pi\hbar)$, calculated for $\varepsilon_F = 2\Omega_O$, $\lambda_0 = 0.5$, $\gamma = 0$, and for several values of $\theta = k_B T/\Omega_O$, presented in different colors.

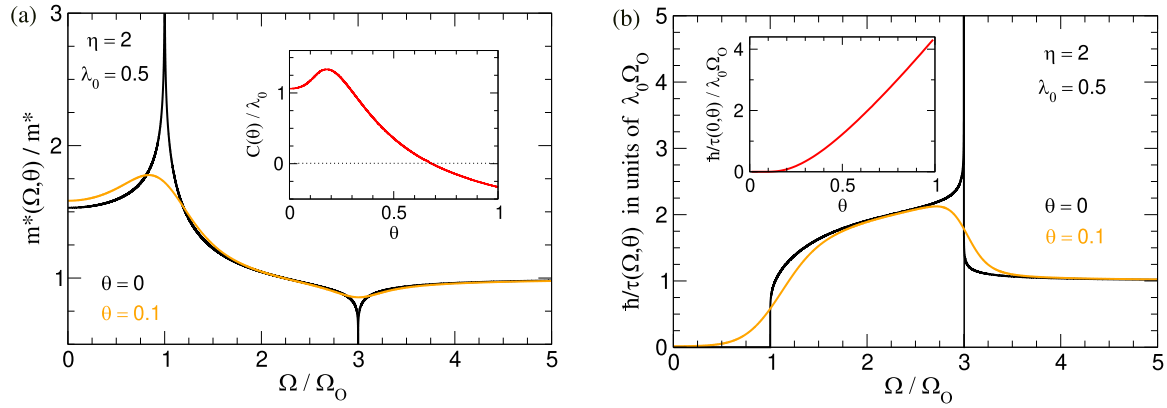

FIG. 5. (a) The dynamical effective mass (5.7) as a function of photon energy Ω, plotted for two different temperatures, and parameters $\lambda_0 = 0.5$ and $\eta = 2$. The inset shows the slope of the low-energy part of the real part of the memory function, in units of λ_0, as it depends on θ. (b) The inverse dynamical relaxation time, plotted as a function of photon energy, for two temperatures and for parameters $\lambda_0 = 0.5$ and $\eta = 2$. The inset shows θ-dependence of the static inverse relaxation time $\hbar/\tau(0,\theta)$ in units of $\lambda_0\Omega_O$.

We conclude that the search for the signatures of the Holstein system in the optical conductivity are best to be performed on very low temperatures. Some of these signatures are the onset of the characteristic hump-like feature in the real part of the dynamical conductivity at photon energy Ω_O and the spike at energy Ω_R. An additional problem for a spike identification is that, in the normal conductors, where $\varepsilon_F \gg \Omega_O$ implies that $\Omega_R \gg \Omega_O$. This increases the possibility that other higher-energy phonons influence the dynamical conductivity and that we may cross the boundaries of the model applicability as stated in Sec. IV A.

A. Extended Drude model

The generalized Drude formula Eqs. (2.4) or (5.1) has an alternative way of representation. Historically, this representation is called the extended Drude model [12,59,60] and is often used in the analysis of the far-infrared conductivity. Setting $\gamma = 0$, for the 2D wdH, it reads

$$\sigma(\Omega,\theta) = \frac{ie^2}{m^*(\Omega,\theta)}\frac{n}{\Omega + i\hbar/\tau(\Omega,\theta)}, \tag{5.6}$$

and it is completely analogous to Eq. (5.1) under the assumption that an electron band is parabolic, so we can use the total concentration of electrons $n = m^*\varepsilon_F/(\pi\hbar^2)$ instead of the effective concentration n_α (4.1). It is trivial to show that the dynamic effective electron mass $m^*(\Omega,\theta)$ and the dynamic relaxation time $\tau(\Omega,\theta)$ are defined with respect to the real and imaginary parts of the memory function as

$$\frac{m^*(\Omega,\theta)}{m^*} = 1 + \frac{\hbar M_1(\Omega,\theta)}{\Omega}, \qquad \frac{\hbar}{\tau(\Omega,\theta)} = \frac{\hbar M_2(\Omega,\theta)}{m^*(\Omega,\theta)/m^*}. \tag{5.7}$$

The above quantities are shown in Figs. 5(a) and 5(b) for the specific cases of $\eta = 2$ and $\lambda_0 = 0.5$ as functions of photon energy Ω.

As defined in Eq. (5.7), $m^*(\Omega,0)$ retains the logarithmic divergences at points Ω_O and Ω_R, which are then smoothed out under a finite temperature, but asymptotically approaches $m^*(\Omega \gg \Omega_R, 0)/m^* \to 1$. In the low $\Omega \ll 1$ regime we tend to introduce the static electron mass renormalization due to the interaction with the optical phonon. We showed in Sects. IV A and IV B that, in this regime, for any temperature θ, $\hbar M_1(\Omega \ll \Omega_O, \theta) \approx C(\theta)\Omega$ where $C(\theta = 0) = \lambda_0(2/\pi)(1+2\eta)/(1+\eta)$ is determined by Eq. (4.9), i.e., the measuring of $C(0)$ determines the electron-phonon coupling λ_0. Hence, we can trace out how the static mass of the transport electron changes with temperature, i.e., $m^*(0,\theta)/m^* = 1 + C(\theta)$, with the slope $C(\theta)$ shown in the inset of Fig. 5(a).

The inverse zero-θ dynamical relaxation time $\hbar/\tau(\Omega,0)$ diverges at points $\Omega^*_{1,2}$ (see Sec. V) to positive and at Ω_R to negative infinity. This property is inherited from $M_{1,2}(\Omega,0)$ as is the hump-like feature at Ω_O like the one found in $\sigma_1(\Omega_O,0)$, as shown in Fig. 5(b). Again, the finite θ smears the onset and the divergence. In the high-energy limit, $\Omega \gg \Omega_R$, it approaches Eq. (4.13). The temperature dependence of its static part deviates from the linear result which was found for $M_2(0,\theta) \sim \theta$, as shown in the inset of Fig. 5(b) due to $C(\theta)$.

With the help of formula (5.6), we can obtain the DC zero-temperature spectral weight. There is no relaxation below Ω_O at $\theta = 0$, Fig. 5(b), and the $\hbar/\tau(\Omega < \Omega_O, 0)$ can be thought of as being an infinitesimal constant ϵ. With the help of an identity $-i\pi\delta(\Omega) = \lim_{\epsilon\to 0}(\Omega + i\epsilon)^{-1}$ Eq. (5.6) reduces to

$$\sigma_1(\Omega < \Omega_O, 0) = \frac{\pi\sigma_0\varepsilon_F}{1 + C(0)}\,\delta(\Omega). \tag{5.8}$$

Thus the Drude weight [61], as it is called, is reduced since $m^*(0,0) > m^*$. This is also shown in Fig. 3(a) for a finite γ case. Since the total spectral weight (5.4) is conserved, we can determine the contribution of the hump-like structure in $\sigma_1(\Omega,0)$, Fig. 3, in the sum rule

$$\int_{\Omega_O}^{\infty} \sigma_1(\Omega,0)d\Omega = \frac{\pi}{2}\frac{C(0)}{1+C(0)}\sigma_0\varepsilon_F. \tag{5.9}$$

If the interband contributions to $\sigma_1(\Omega)$, as well as other phonons, are far away in energy, even at finite θ, as long as the hump above Ω_O is well defined, Eq. (5.9) can be used to extrapolate the basic data about the electron-phonon interaction in the system [62].

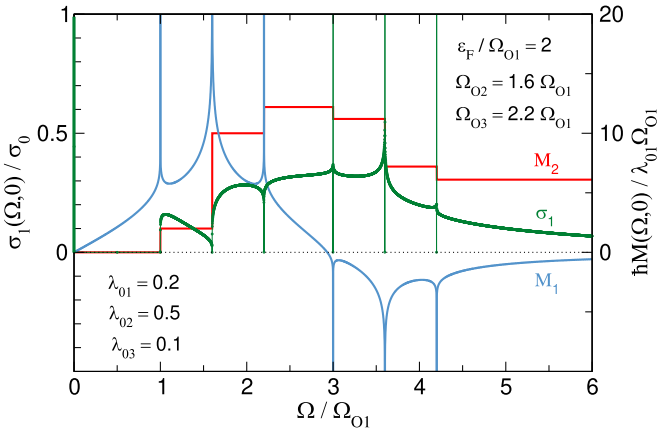

FIG. 6. The real (blue) and the imaginary (red) part of the total zero-temperature memory function (5.10) as a function of photon energy. The real part of the zero-temperature dynamical conductivity Eq. (5.2) (green) calculated using the memory function from the same figure, setting $\gamma = 0$.

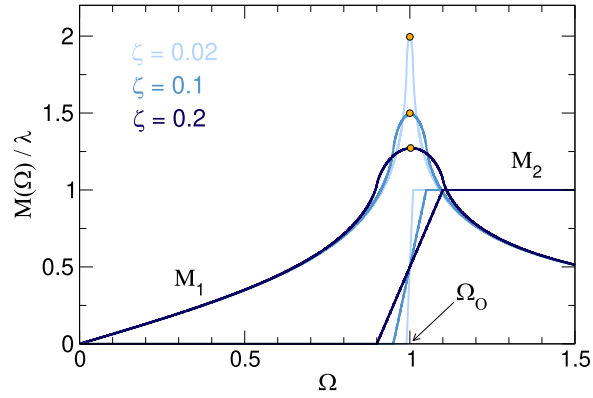

FIG. 7. The real part (A2) and the imaginary part (A1) of the low-temperature memory function model as function of Ω as it depends on parameter ζ.

B. Conductivity of a wdH system with multiple phonon branches

We can generalize the memory function approach to obtain the dynamical conductivity of conducting electrons when multiple phonon branches are present. The scattering mechanism on each of them is of the Holstein type (2.3) under the condition that the maximal phonon energy and the incoming photon energy obey the restriction of the model as given in Sec. IV A. Up to the second order in the electron-phonon interaction, the total memory function is just a sum of individual memory functions which describe scattering on all types of phonons (2.6). The parameters, which are characteristic for every optical phonon branch indexed by i, are the optical phonon energy Ω_{Oi} and the coupling matrix element $G(\Omega_{Oi})$. Similar to Eq. (4.3) we define $\hbar\lambda_i = \lambda_{0i}\Omega_{Oi}$, so we get

$$\hbar M_{1,2}^{\text{tot}}(\Omega, T) = \sum_{\Omega_O} \hbar M_{1,2}(\Omega, T). \tag{5.10}$$

For the wdH type of system, for demonstration purposes, we take the $T = 0$ case and use the expressions (4.7) and (4.8) to define the total memory function in Eq. (5.10). We assume that there are three optical phonons in the system at energies Ω_{O1}, $\Omega_{O2} = 1.6\Omega_{O1}$, $\Omega_{O3} = 2.2\Omega_{O1}$ with the corresponding dimensionless couplings $\lambda_{01} = 0.2$, $\lambda_{02} = 0.5$, $\lambda_{03} = 0.1$, respectively (not related with 2D MoS_2). Using the scaling analogous as before the plot of memory function is shown in Fig. 6. As expected M_2^{tot} turns into a set of steps at the corresponding energies, step-up at Ω_{Oi} and step-down at $\Omega_{Ri} = \Omega_{Oi} + \varepsilon_F$. At those points the real part of the total memory function attains logarithmic singularities, and is positive along the "step-up interval" and negative along the "step-down interval." The DC response (thick green line) is given by Eq. (5.8), where instead of $C(0)$ we use the sum of individual contributions $\sum_i C_i(0)$ which also appears in the hump-like spectral weight (5.9). The finite temperature, if $\theta < k_B T/\Omega_{O1}$, does not smear the high-energy part of the total multiphonon $\sigma_1(\Omega, \theta)$. In this case, some of its fine features (concavity on certain intervals and spikes or dips) may be accessible to experimental verification.

VI. CONCLUSION

We use the generalized Drude model to find the dynamical conductivity of a two-dimensional system in which conducting electrons with a parabolic-like band dispersion scatter on a dispersionless optical phonon. The goal is to investigate the real part of conductivity of such a system when all relevant energy scales, such as the Fermi energy, optical phonon energy, photon energy, and temperature are comparable. The memory function used in this paper assumes that Fermi-Dirac and Bose-Einstein distributions are given by their equilibrium values and are not affected by the electron and phonon single-particle energy renormalization. Properties of the zero-temperature memory function with different Fermi to optical phonon energy ratios have been studied in detail. Most notable features of the zero-temperature real part of the dynamical conductivity are the onset of a hump-like structure at the optical phonon energy and the finite narrow spike located at the energy equal to the sum of the Fermi energy and optical phonon energy. Finite-temperature memory function is presented, especially its temperature evolution as the temperature is increased from zero to the energy equivalent to that of the optical phonon. Finally, the finite-temperature dynamical conductivity is calculated with several experimentally observable features identified. Those include the charge conservation (the sum rule), the DC resistivity, and the bordering temperature above which conductivity resembles the one given by a simple Drude model. A connection between the generalized and extended Drude model is made by relating the dynamical effective mass and the relaxation time to the memory function. Also, it has been shown how to determine the relevant electron-phonon coupling from the sum rule. Due to the additive property of the memory function, a case of the zero-temperature dynamical relaxation of conducting electrons on multiple optical phonon branches has been investigated, as well as the effect it has on the dynamical conductivity. It is done under the assumption that acoustic and other optical modes, which do not couple to electrons via Holstein coupling, are energetically well separated from the

optical phonon modes which do. In this case, the spikes and the dips in the extremely low-temperature conductivity could be observed and their shift with doping could be an indicator that the system is low-doped Holstein-like (in contrast to standard systems with Fermi energy much larger then phonon energy where those features do not appear). This, on the other hand, would be a confirmation that the electron and phonon energy renormalization effects, which modify the fermion and boson distributions, are indeed small.

ACKNOWLEDGMENTS

This work was supported by the QuantiXLie Centre of Excellence, a project cofinanced by the Croatian Government and European Union through the European Regional Development Fund—the Competitiveness and Cohesion Operational Program (Grant No. KK.01.1.1.01.0004).

APPENDIX: $\theta \ll 1$ MODEL MEMORY FUNCTION

Here we present a simple model of a low-temperature $k_BT \ll \Omega_O$ behavior of the imaginary and real parts of the memory function. Based on the finite-temperature analysis in Sec. IV B, the $M_2(\Omega)$ is modeled as a nearly step-function with the middle of a step located at Ω_O with finite slope between the points Ω_1 and Ω_2, as shown in Fig. 7

$$M_2(\Omega) = \lambda \times \begin{cases} 0, & \Omega < \Omega_1, \\ (\Omega - \Omega_1)/(\Omega_2 - \Omega_1), & \Omega_1 < \Omega_O < \Omega_2, \\ 1, & \Omega_2 < \Omega. \end{cases} \tag{A1}$$

Using the KKR, the real part of the memory function is obtained

$$\frac{\pi}{\lambda} M_1(\Omega) = \frac{\Omega - \Omega_1}{\Omega_2 - \Omega_1} \ln \left| \frac{\Omega_2 - \Omega}{\Omega_1 - \Omega} \right| + \frac{\Omega + \Omega_1}{\Omega_2 - \Omega_1} \ln \left| \frac{\Omega_2 + \Omega}{\Omega_1 + \Omega} \right| + \ln \left| \frac{\Omega_2 + \Omega}{\Omega_1 - \Omega} \right|, \tag{A2}$$

which is plotted in Fig. 7 for three cases of $\zeta \equiv \Omega_2 - \Omega_1$. If we are interested in the value of $M_1(\Omega_O)$ as a function of $\zeta \to 0$, we set $\Omega = \Omega_O = (\Omega_2 + \Omega_1)/2 = \Omega_1 + \zeta/2$, and insert it into Eq. (A2). The first term vanishes, the second term gives

$$\lim_{\zeta \to 0} \ln (1 + \zeta/2\Omega_O)^{2\Omega_O/\zeta} = 1, \tag{A3}$$

while the third gives $\ln 4\Omega_O/\zeta$. Combining them together we get

$$M_1(\Omega_O) = \frac{\lambda}{\pi} \ln \frac{4e\Omega_O}{\zeta}, \tag{A4}$$

as indicated by the orange circles in Fig. 7. The connection with $M_1(\theta \ll 1, \Omega_O)$ follows by setting $\zeta \approx \theta$.

[1] N. W. Ashcroft and N. D. Mermin, *Solid State Physics* (Brooks-Cole, Pacific Grove, CA, 1976).
[2] S. Uchida, T. Ido, H. Takagi, T. Arima, Y. Tokura, and S. Tajima, Phys. Rev. B **43**, 7942 (1991).
[3] S. I. Mirzaei, D. Stricker, J. N. Hancock, C. Berthod, A. Georges, E. van Heumen, M. K. Chan, X. Zhao, Y. Li, M. Greven, N. Barišić, and D. van der Marel, Proc. Natl. Acad. Sci. USA **110**, 5774 (2013).
[4] I. Kupčić and I. Jedovnicki, Eur. Phys. J. B **90**, 63 (2017).
[5] I. Kupčić, Phys. Rev. B **91**, 205428 (2015).
[6] I. Kupčić, Phys. Rev. B **95**, 035403 (2017).
[7] Z. Rukelj, Phys. Rev. B **102**, 205108 (2020).
[8] P. Bhalla, P. Kumar, N. Das, and N. Singh, J. Phys. Chem. Solids **109**, 31 (2017).
[9] W. Götze and P. Wölfle, Phys. Rev. B **6**, 1226 (1972).
[10] P. B. Allen, Phys. Rev. B **3**, 305 (1971).
[11] B. Mitrović and M. A. Fiorucci, Phys. Rev. B **31**, 2694 (1985).
[12] S. V. Shulga, O. V. Dolgov, and E. G. Maksimov, Physica C: Supercond. **178**, 266 (1991).
[13] P. B. Allen, Phys. Rev. B **92**, 054305 (2015).
[14] L. Rani and N. Singh, J. Phys.: Condens. Matter **29**, 255602 (2017).
[15] P. Bhalla and N. Singh, Int. J. Mod. Phys. B **33**, 1950128 (2019).
[16] W. G. Baber, Proc. R. Soc. London A **158**, 383 (1937).
[17] J. Appel, Phys. Rev. **122**, 1760 (1961).
[18] P. F. Maldague and C. A. Kukkonen, Phys. Rev. B **19**, 6172 (1979).
[19] W. Kohn and J. M. Luttinger, Phys. Rev. **108**, 590 (1957).
[20] P. Bhalla, N. Das, and N. Singh, Phys. Lett. A **380**, 2000 (2016).
[21] P. Bhalla, Phys. Lett. A **381**, 924 (2017).
[22] T. Holstein, Ann. Phys. (NY) **8**, 325 (1959).
[23] S. Ragni, T. Hahn, Z. Zhang, N. Prokof'ev, A. Kuklov, S. Klimin, M. Houtput, B. Svistunov, J. Tempere, N. Nagaosa, C. Franchini, and A. S. Mishchenko, Phys. Rev. B **107**, L121109 (2023).
[24] T. Hahn, N. Nagaosa, C. Franchini, and A. S. Mishchenko, Phys. Rev. B **104**, L161111 (2021).
[25] J. Krsnik, I. Batistić, A. Marunović, E. Tutiš, and O. S. Barišić, Phys. Rev. B **102**, 241111(R) (2020).
[26] B. Pandey and P. B. Littlewood, Phys. Rev. Lett. **129**, 136401 (2022).
[27] C. Zhang, E. Jeckelmann, and S. R. White, Phys. Rev. B **60**, 14092 (1999).
[28] O. S. Barišić, Phys. Rev. B **73**, 214304 (2006).
[29] D. Jansen, J. Stolpp, L. Vidmar, and F. Heidrich-Meisner, Phys. Rev. B **99**, 155130 (2019).
[30] A. S. Mishchenko, N. Nagaosa, G. De Filippis, A. de Candia, and V. Cataudella, Phys. Rev. Lett. **114**, 146401 (2015).
[31] G. L. Goodvin, A. S. Mishchenko, and M. Berciu, Phys. Rev. Lett. **107**, 076403 (2011).
[32] G. Grimvall, *The Electron-Phonon Interaction in Metals* (North-Holland, Amsterdam, 1981).

[33] V. V. Kabanov, J. Phys. Commun. **6**, 115002 (2022).
[34] J. Bonča and S. A. Trugman, Phys. Rev. B **106**, 174303 (2022).
[35] J. Loos, M. Hohenadler, A. Alvermann, and H. Fehske, J. Phys.: Condens. Matter **19**, 236233 (2007).
[36] C. Grimaldi, L. Pietronero, and M. Scattoni, Eur. Phys. J. B **10**, 247 (1999).
[37] D. Jansen, J. Bonča, and F. Heidrich-Meisner, Phys. Rev. B **106**, 155129 (2022).
[38] E. Jeckelmann and S. R. White, Phys. Rev. B **57**, 6376 (1998).
[39] S. Fratini, F. de Pasquale, and S. Ciuchi, Phys. Rev. B **63**, 153101 (2001).
[40] G. Schubert, G. Wellein, A. Weisse, A. Alvermann, and H. Fehske, Phys. Rev. B **72**, 104304 (2005).
[41] S. Moser, L. Moreschini, J. Jaćimović, O. S. Barišić, H. Berger, A. Magrez, Y. J. Chang, K. S. Kim, A. Bostwick, E. Rotenberg, L. Forró, and M. Grioni, Phys. Rev. Lett. **110**, 196403 (2013).
[42] C. Verdi, F. Caruso, and F. Giustino, Nat. Commun. **8**, 15769 (2017).
[43] J. Krsnik, V. N. Strocov, N. Nagaosa, O. S. Barišić, Z. Rukelj, S. M. Yakubenya, and A. S. Mishchenko, Phys. Rev. B **102**, 121108(R) (2020).
[44] Z. Rukelj, A. Štrkalj, and V. Despoja, Phys. Rev. B **94**, 115428 (2016).
[45] Z. Li and J. P. Carbotte, Phys. Rev. B **86**, 205425 (2012).
[46] K. Kaasbjerg, K. S. Thygesen, and K. W. Jacobsen, Phys. Rev. B **85**, 115317 (2012).
[47] Z. Li and J. P. Carbotte, Phys. B: Condens. Matter **421**, 97 (2013).
[48] H. Rostami and R. Asgari, Phys. Rev. B **89**, 115413 (2014).
[49] T. Gunst, T. Markussen, K. Stokbro, and M. Brandbyge, Phys. Rev. B **93**, 035414 (2016).
[50] Z. Li, G. Antonius, M. Wu, F. H. da Jornada, and S. G. Louie, Phys. Rev. Lett. **122**, 186402 (2019).
[51] Z. Rukelj and A. Akrap, Phys. Rev. B **104**, 075108 (2021).
[52] Z. Rukelj and D. Radić, Condens. Matter. **8**, 1 (2023).
[53] D. Novko, Commun. Phys. **3**, 30 (2020).
[54] Z. Li and J. P. Carbotte, Eur. Phys. J. B **88**, 87 (2015).
[55] G. D. Mahan, *Many-Particle Physics* (Springer, New York, 2000).
[56] J. Tempere and J. T. Devreese, Phys. Rev. B **64**, 104504 (2001).
[57] A. Molina-Sánchez and L. Wirtz, Phys. Rev. B **84**, 155413 (2011).
[58] J. M. Ziman, *Electrons and Phonons: The Theory of Transport Phenomena in Solids* (Oxford University Press, Oxford, UK, 2001).
[59] T. Timusk, Solid State Commun. **127**, 337 (2003).
[60] F. Marsiglio, T. Startseva, and J. P. Carbotte, Phys. Lett. A **245**, 172 (1998).
[61] D. J. Scalapino, S. R. White, and S. Zhang, Phys. Rev. B **47**, 7995 (1993).
[62] D. N. Basov, R. D. Averitt, D. van der Marel, M. Dressel, and K. Haule, Rev. Mod. Phys. **83**, 471 (2011).